Characterization of antiphase boundary network in $Fe_3O_4(111)$ epitaxial thin films: Effect on anomalous magnetic behavior

A. M. Bataille,[*] L. Ponson, S. Gota,[†] L. Barbier, D. Bonamy, and M. Gautier-Soyer

DRECAM/SPCSI, CEA Saclay, 91191 Gif-sur-Yvette, France

C. Gatel and E. Snoeck

CEMES-CNRS/Nanomat, 19 rue Jeanne Marvig, 31055 Toulouse Cedex 4, France

(Received 20 May 2006; revised manuscript received 30 August 2006; published 30 October 2006)

We report on the antiphase boundaries network of $Fe_3O_4(111)$ thin films. 5- to 50-nm-thick samples were epitaxially grown by molecular beam epitaxy onto α-$Al_2O_3(0001)$ substrates. The magnetic properties of the samples have been interpreted within the framework of a one-dimensional model of antiphase boundary (APB), which predicts that the magnetization is given by $M_\infty(1-b/\sqrt{H})$ in the approach to saturation regime. Transmission electron micrographs of several samples were used to extract the statistical parameters of the APB network, particular emphasis being put on the relevance and statistical significance of the studied parameters. The mean antiphase domain size $\bar{D}$, as the antiphase boundaries characteristic length l_0 extracted from a fractal analysis, vary as the square root of film thickness/deposition time and are within the 10 nm range. The APB density was found to vary as $1/l_0$ as expected from the fractal dimensions of the network. The dependency of the b parameter of the magnetic model on the APB density is finally analyzed in the light of micromagnetic simulations of chains including finite size antiphase domains and two APBs.

I. INTRODUCTION

Considerable interests have been devoted to the study of magnetic thin films over the last decade since they play a crucial role in spin valves,[1] magnetic tunnel junctions,[2,3] and, more generally, in spin electronics devices.[4] A class of materials particularly helpful[5] for the understanding of the physics of the spin electronics devices is made of the so-called half-metals, which are fully spin polarized, i.e. conductors for one spin direction and insulators for the other. Transport and photoemission experiments have demonstrated that CrO_2 (Ref. [6]) and the perovskites $La_xSr_{1-x}MnO_3$ (Refs. [7] and [8]) and $SrFe_2MoO_6$ (Ref. [9]) are indeed half-metallic, but only at low temperature. The spinel Fe_3O_4 (magnetite) appears thus quite interesting,[10,11] since band structure calculations have predicted a half metallic behavior,[12–14] and it might exhibit high spin polarization at 300 K, or above, given its high Curie temperature (T_C=860 K).

However, the amplitude of the giant magnetoresistance[15,16] or tunnel magnetoresistance[17–26] of devices including Fe_3O_4 measured to date is much lower than expected from the predicted half metallic character of the compound. The origin of this discrepancy is not fully understood yet but part of the explanation is probably to be found in the significant differences between the magnetic properties of Fe_3O_4 thin films and those of bulk samples.[25,26] One of the puzzling features of the magnetic behavior of Fe_3O_4 thin films is the lack of saturation even under large applied fields (up to 70 kOe).[27,28] This has been qualitatively ascribed to the presence of the antiphase boundaries (APBs) which are structural defects that delimitate the symmetry invariant domains (variants) of the sample. Such APBs are present in various compounds including bimetallic alloys [e.g. Cu_3Au (Ref. [29]) or Fe_xAl_{1-x} (Refs. [30] and [31])] and oxides.[32,33] There are eight equivalent cation sublattices for a given oxygen sublattice in the spinel structure into which Fe_3O_4

crystallizes, but from a practical point of view, the symmetry operation required to transform one of these sublattices into another is equivalent to a translation of a vector of the $1/4$ $\langle 110 \rangle$ family or one of their linear combinations. Although APBs have also been observed in bulk spinels,[32] they are mostly associated with Fe_3O_4 thin films and more specifically with the coalescence of islands exhibiting different cation sublattices.[34] It is worth noting that APBs have been observed in Fe_3O_4 thin films epitaxially grown onto a great variety of substrates, e.g. MgO,[27,34–37] α-Al_2O_3,[38–40] Pt,[41] and even the original spinel $MgAl_2O_4$.[42] This is suprising since some of the shift vectors should be forbidden depending on the symmetry of the substrate, in particular in the case of $MgAl_2O_4$ where the identical structure of the substrate and the film should lead to growth without APBs. The APB network was first thought to be set during the very first stages of growth,[34] but a systematic study demonstrated that the size of antiphase domain increases both with film thickness and annealing time.[35]

The influence of APBs on magnetic properties comes from the existence of specific geometries of the Fe-O-Fe arrangements not present in perfect Fe_3O_4 crystalline structure.[27,43] Since superexchange depends strongly on the angle between the Fe-O bonds, one expects specific magnetic couplings at some of the APBs. The exact evaluation of such couplings at a given type of APB (defined by two parameters, the shift vector and the boundary plane) is made difficult because of the numerous Fe-O-Fe bonds which should be taken into account and the lack of quantitative information available on superexchange;[43] the Goodenough-Kanamori rules[44,45] give only qualitative results and concern solely particular geometries. However, a given fraction of APBs comprise aligned Fe^{3+}-O-Fe^{3+} bonds which are known to create extremely strong antiferromagnetic superexchange.[46] The resulting coupling is thus expected to be

strongly antiferromagnetic at these APBs, which are considered to be responsible for the lack of the saturation in Fe_3O_4 thin films. The proportion of such antiferromagnetic APBs is not known in general since it depends on distribution of the boundary plane–shift vector couples, which in turns depends on the substrate and growth orientation used. A proportion of 10 to 20 % has been reported for Fe_3O_4(100) grown on MgO.[47,48]

In a previous paper[38] we adapted a one-dimensional model initially developed for Fe/Gd multilayers[49] to describe the approach to saturation in Fe_3O_4 thin films. However, this study was only semiquantitative: It did not account for the variation of APB density. In this paper, we carry out a thorough quantitative analysis of the APB network to further analyze magnetic data.

The paper is organized as follows. The experimental setup and image binarization process are described in Sec. II. In Sec. III, the experimental results are displayed. Magnetism data are analyzed using the one dimensional model of Ref. 38 and the procedure used to extract the parameters that characterize the morphology of the APB network are presented. In particular, we present a fractal analysis method which, aside from extracting the APB characteristic length acertain the relevance of APB density values extracted from the image analysis. Growth mode and magnetic properties are discussed in the light of the statistical analysis and micromagnetic simulations in Sec. IV.

II. EXPERIMENTS

Samples were grown using an oxygen-assisted molecular beam epitaxy setup described in detail elsewhere[38,50] and briefly summarized below. Fe_3O_4(111) layers with thickness ranging from 5 to 50 nm were deposited onto sapphire (0001) substrates at a temperature of 450 °C and a pressure lower than 2×10^{-8} mbar (base pressure $< 2 \times 10^{-10}$ mbar). The growth is then achieved by evaporating metallic Fe from a Knudsen effusion cell under atomic oxygen generated by a rf plasma source (atomic oxygen partial pressure in the growth chamber $= 8 \times 10^{-9}$ mbar, atomic oxygen flow in the 10^{13} atoms $cm^{-2} s^{-1}$ range). Deposition rates are measured *in situ* using a quartz balance and checked *ex situ* by x-ray reflectivity: Both methods lead to a growth rate of 0.18 nm $min^{-1} \pm 5\%$. The growth remains two-dimensional (2D) during the whole process as demonstrated by reflected high energy electron diffraction (RHEED) patterns (shown in Ref. 50) recorded during the deposition.

The magnetic properties of the samples were measured at room temperature using a commercial vibrating sample magnetometer (VSM) manufactured by the ADE company. The field was applied in the plane of the films, along the $\langle 1\bar{1}0 \rangle$ direction of the Fe_3O_4 lattice (no in plane anisotropy has been observed for all the samples). Special attention was paid to determine the diamagnetic contribution of the α-Al_2O_3 substrate by measuring the magnetic signal for each substrate before Fe_3O_4 deposition. This signal was then subtracted from the one of the complete sample, so that the magnetic signal of the sole Fe_3O_4 thin film is obtained.
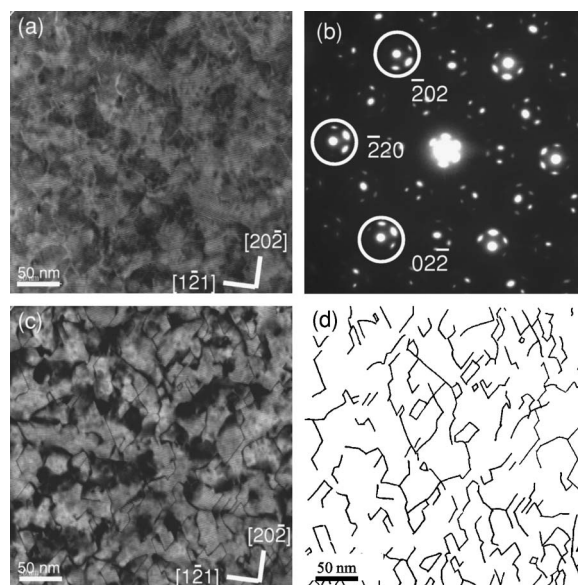

FIG. 1. Example of 325×325 nm^2 TEM bright and dark field images of a 32-nm-thick Fe_3O_4 thin film. (a) Bright field. Part of the APBs are barely visible as white lines. (b) Selected area diffraction pattern. The circles correspond to the three 220 type reflections allowed with this zone axis. (c) Dark field image obtained after selecting the $02\bar{2}$ reflection. Two third of the APBs have a shift component perpendicular to the $02\bar{2}$ plane selected for the dark field image and appear as black lines. The remaining third is not visible on this micrograph but would become apparent by using another 220 reflection for the dark field acquisition. (d) APB network as obtained after the "manual binarization" step (see text for details).

Thin samples were prepared for transmission electron microscopy (TEM) analysis from films of four different thicknesses (8, 15, 32, and 50 nm), using the usual mechanical polishing and ion thinning techniques. TEM experiments were performed using a CM30 LaB$_6$ microscope on plane view samples, i.e. studied with the *e*-beam parallel to the growth direction. Specific information can be gathered by TEM when performing dark field measurements, as illustrated in Fig. 1. Figure 1(a) displays a typical bright field image of a 32-nm-thick Fe_3O_4 thin film studied along a [111] zone axis. The diffraction pattern is shown in Fig. 1(b). The circles indicate the three $\bar{2}20$, $\bar{2}02$, and $02\bar{2}$ reflections (110 reflections are forbidden in the spinel structure) surrounded by six satellites. The latter are due to double diffraction phenomenon due to the *e*-beam that has been successively diffracted by the α-Al_2O_3 and Fe_3O_4 superimposed crystals. The micrograph in Fig. 1(c) is the dark field image obtained selecting the Fe_3O_4 $02\bar{2}$ reflection. APBs can be indeed considered as stacking faults of shift vectors of the 1/4 $\langle 110 \rangle$ type, four out of these six vectors breaking the periodicity of the particular (220) planes. Assuming a homogeneous distribution of APB (one sixth of the APBs for any of the six 1/4 $\langle 110 \rangle$ vectors), each dark field image such as Fig. 1(c) shows two thirds of the APB network.

The resulting dark field images are then binarized [Fig. 1(d)]. This step has proven to be difficult, particularly because of the Moiré pattern (originating from the existence of
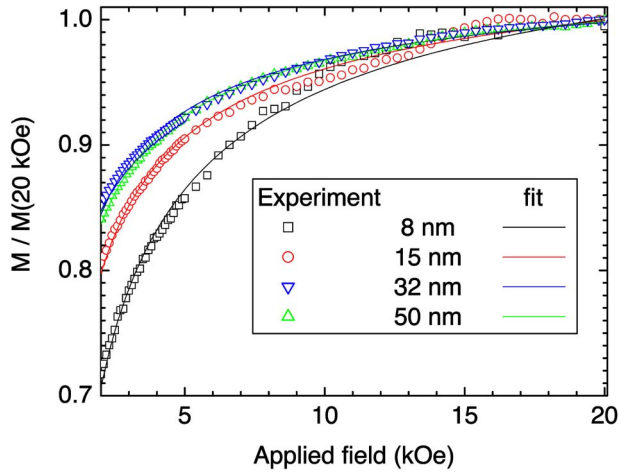
FIG. 2. (Color online) Examples of virgin magnetization curves obtained for films of different thicknesses, and best fits obtained with Eq. (2).
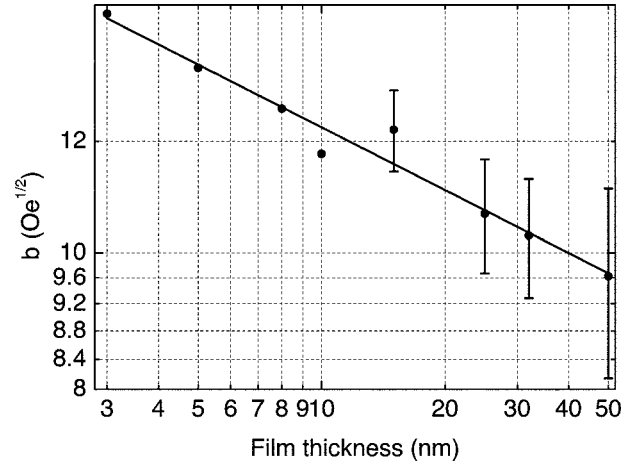

FIG. 3. b parameter as a function of film thickness, represented using a log-log scale. Error bars correspond to the standard deviation calculated when several samples of the same thickness have been grown and measured. The straight line represents the best power law fit, with a -0.15 ± 0.01 exponent.

two superimposed periodic structures, the α-Al_2O_3 substrate and the Fe_3O_4 thin film) present on each picture. We were not able to design an efficient automated binarization procedure and finally choose to perform this task manually by reproducing the APB network on a semitransparent paper and numerizing the resulting drawing. The resulting image was then binarized and a skeletization process was applied so that APBs appear as 1D lines on the final image.

III. EXPERIMENTAL RESULTS

A. Magnetization curves analysis

Although full hysteresis loops have been systematically measured on all samples, we will focus in this paper on virgin magnetization measurements only, in order to study the approach to saturation. Figure 2 displays a few examples of such curves. The magnetization of each sample has been normalized by $M(H=20 \text{ kOe})$, this value corresponding to the largest applied field in our apparatus.

These curves were analyzed using the model described in details in Refs. 26 and 38, which we briefly summarize here. This model considers two antiferromagnetically coupled semi-infinite chains, exchange and Zeeman terms being the only magnetic interactions taken into account (the magnetic anisotropy is neglected, so the field direction with respect to the crystallographic axes is not specified in the model). In this framework, the magnetization loss ΔM of an *individual* infinite chain (equivalent to the magnetization loss per surface unit of boundary) along the direction of the applied field $\vec{H}$ can be obtained analytically and is given by

$$\Delta M(H) = M_0 \left(1 - 2\sqrt{\frac{A_F}{a^2 M_0 H}} (1 - \sqrt{2}) \right), \quad (1)$$

where M_0 is the theoretical saturation magnetization, a the distance between adjacent chains in the boundary and A_F the exchange stiffness between two neighboring spins (note that since Fe_3O_4 is a ferrimagnet, A_F is a mean value calculated from the different exchange constants; an *effective* value of

A_F can be obtained from torque measurements[51]). The field dependence of the *total* magnetization is then assumed to be similar to the one of the individual chain given by Eq. (1), and the experimental curves can be fitted with two parameters using

$$M(H) = M_\infty \left(1 - \frac{b}{\sqrt{H}} \right), \quad (2)$$

where M_∞ is the saturation magnetization and b a parameter measuring the difficulty of the approach to saturation (the relation between b and the APB density will be discussed in the last section of this paper).

This last equation was used to fit the magnetization curves of Fig. 2. The $M_\infty / M(20 \text{ kOe})$ ratio was found to be nearly constant, varying between 1.05 and 1.1 without any obvious thickness dependence. The evolution of the b parameter, characterizing the *shape* of the $M(H)$ curve, is shown in Fig. 3. b depends weakly but clearly on the thickness, the data being reproduced in coarse approximation by a power law of exponent 0.15 ± 0.01. The values are of the same order of magnitude as those reported by the literature,[52] yet slightly larger than those reported for $Fe_3O_4(100)$ films grown on MgO of comparable thickness, probably because of differences in the APB network geometry, the fraction of APBs exhibiting antiferromagnetic couplings and/or the APB density.

B. Angular analysis

Two-dimensional power spectra (Fourier transforms of the 2D autocorrelation functions, which are also the square module of the Fourier transforms of the original images) were calculated in order to study the directionality of the APB network. Typical results are displayed in Fig. 4. The spectra are all "X" shaped (it is less clear for the 50-nm-thick film), the two branches corresponding to $\langle 110 \rangle$ directions, separated by 60°. There is almost no APBs which boundary
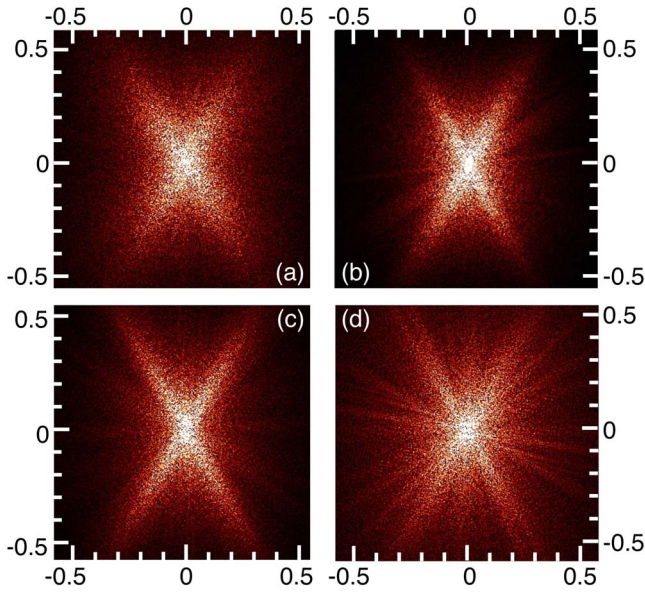
FIG. 4. (Color online) Two-dimensional power spectra of selected binarized images: (a) 8-nm-thick film, (b) 15-nm-thick film, (c) 32-nm-thick film, (d) 50-nm-thick film. Images have been rotated so that the horizontal axis corresponds to the direction of the spot selected in order to obtain the dark field image. The scale correspond to the spatial frequency given in nm^{-1}.

FIG. 5. Statistical distribution of the antiphase domain size along an arbitrary direction of a plane view from a 15-nm-thick Fe$_3$O$_4$ film. For this particular direction, we measure 20.6 and 19.7 nm for the mean APD size D and the standard deviation σ_D, respectively. The shaded area corresponds to the $[\bar{D}-\sigma_D,\bar{D}+\sigma_D]$ interval. The inset shows the cumulative probability (straight line) which is fairly well reproduced using an exponential law (dashed line) $C(x)=1-e^{-x/x_0}$, the best fit corresponding to $x_0=20.6$ nm.

plane lies in the remaining ⟨110⟩ direction corresponding to the spot used to make the dark field measurements. This symmetry breaking evidences a correlation between APBs orientations and shift vectors: since the dark filed images used for the analysis show only two thirds of the APBs, the absent lobe in each power spectrum can be associated with the lacking APBs. Such a correlation was found in the prototypical Cu$_3$Au ordered alloy where a preferential orientation of APBs is similarly pointed out. In that case, the APBs are oriented in such a way that there are conservative (i.e., the local stoichiometry is preserved) and of low energy.[53] Similarly, one could expect for the Fe$_3$O$_4$ thin film that APBs are aligned along directions of low energy.

C. Distribution of antiphase domain size

In order to unravel the possible connection of the parameter b with the antiphase domains (APDs), we now investigate the size distribution of APD. Extending the analysis proposed in Ref. 35, domain size distribution has been evaluated versus orientation: along a fixed direction, the number of white pixels between APBs (black lines) along each line of the rotated image is measured (we thus measure the size of APD cuts). In addition to the measure of the average APD size, it should be emphasized that this method allows pointing out the anisotropy of the APDs. Figure 5 shows an example of statistical distribution of APD size which is typical of those obtained for any analysis angle and any binarized image. In this example, the APD size mean value and standard deviation are, respectively, 20.6 and 19.7 nm. For any arbitrary direction of a given image, the cumulative probability (obtained by integrating the probability density) could be
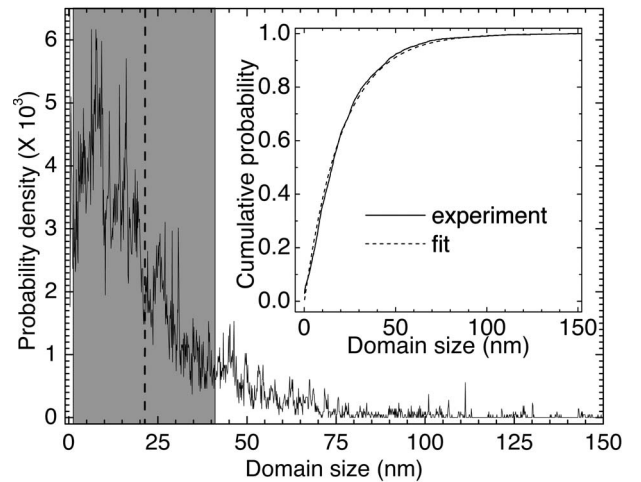
successfully reproduced by an exponential law

$$C(x) = 1 - e^{-x/x_0} \qquad (3)$$

with $x_0=20.6$ nm in our example. This expression of the cumulative probability corresponds to an exponential distribution of the APD sizes

$$P(x) = \frac{1}{x_0}e^{-x/x_0}, \qquad (4)$$

where the x_0 parameter corresponds to the mean value of the distribution.

Such a distribution is reminiscent of the initial Markovian distribution of nucleation centers of APDs. It should also be emphasized that this broad distribution of APD size is characterized by (i) a standard deviation equal to the mean value, (ii) a most likely value different from the mean value, and (iii) distribution parameters depending on the particular direction of the cut. We nonetheless define the mean APD size $\bar{D}$ in the following way: for each direction of a given image, we fit the cumulative APD size distribution with Eq. (3) (see inset of Fig. 5) and then average these x_0 values in order to obtain the mean APD size. The results are displayed in Fig. 6. One observe an increase of the APD size with increasing film thickness, $\bar{D}$ varying as $\sqrt{h}$, average domain size varying from 20 to 40 nm for the film studied in this paper. Yet, as we shall see in Sec. IV, mean APD size alone do not allow us to interpret magnetism data, and the APD size distribution has to be taken into account.

D. Fractal analysis of the antiphase boundary network

We now focus on a deeper description and analysis of the APBs network. To characterize the complex geometry of the
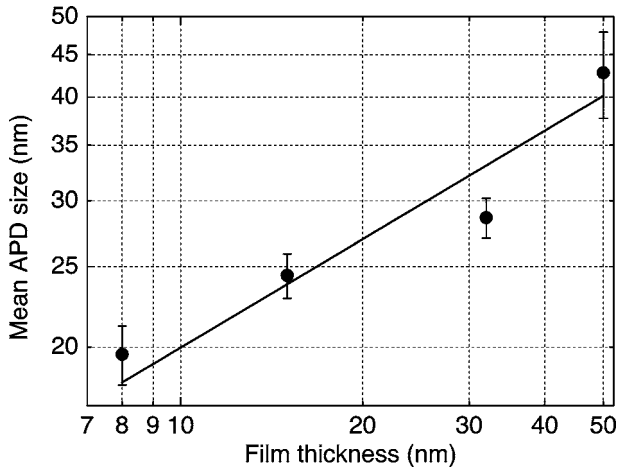
FIG. 6. Mean APD size as a function of film thickness h, represented using a log-log scale. Error bars correspond to the standard deviation calculated from the mean APD size measured on several images of the same sample, and not the standard deviation of the APD size distribution which is equal to the mean value given the statistical law used for the fits. The straight line represents the best power law fit, with a $+0.45 \pm 0.1$ exponent.

APB network, we propose the following fractal analysis which, aside from defining the APB characteristic length, give important information on the relevance of the APB density estimated and discussed in the next section (Sec. III E). Considering a set of N points of coordinates (x_i, y_i), and calling (x_M, y_M) the coordinates of the center-of-mass, the gyration radius R_g is defined by

$$R_g = \sqrt{\frac{1}{N} \sum_{i=1}^{N} [(x_i - x_M)^2 + (y_i - y_M)^2]}. \quad (5)$$

For an object of fractal dimension d_f, N, and R_g are simply related by[54]

$$N \propto R_g^{d_f}. \quad (6)$$

Practically, a set of logarithmically distributed radii $\{R_D\}$ has been chosen at the beginning. For small enough radius R_D, the initial image is divided in subimages of size R_D. One single disk is set within each subimage [Figs. 7(a) and 7(b)], and R_g and N are computed for each disk. For the larger R_D's, overlapping is allowed to achieve better statistics [Fig. 7(c)]. In each of the defined disks, we determined the pixels corresponding to the APB network and calculated the radius of gyration R_g and the number of pixels N as defined in Eq. (5).[26]

Examples of N vs R_g curves are plotted in Fig. 8 for each of the samples studied by TEM. All the samples exhibit a similar behavior consisting of two distinct regimes: for small radii of gyration, the data is reproduced by a power law fit with an exponent close to 1, whereas for large radii of gyration, power law fitting yield to an exponent close to 2 (see Table I). The small scale regime corresponds to the individual objects. The large scale regime describes the geometry of the whole APB network. We thus define the characteristic
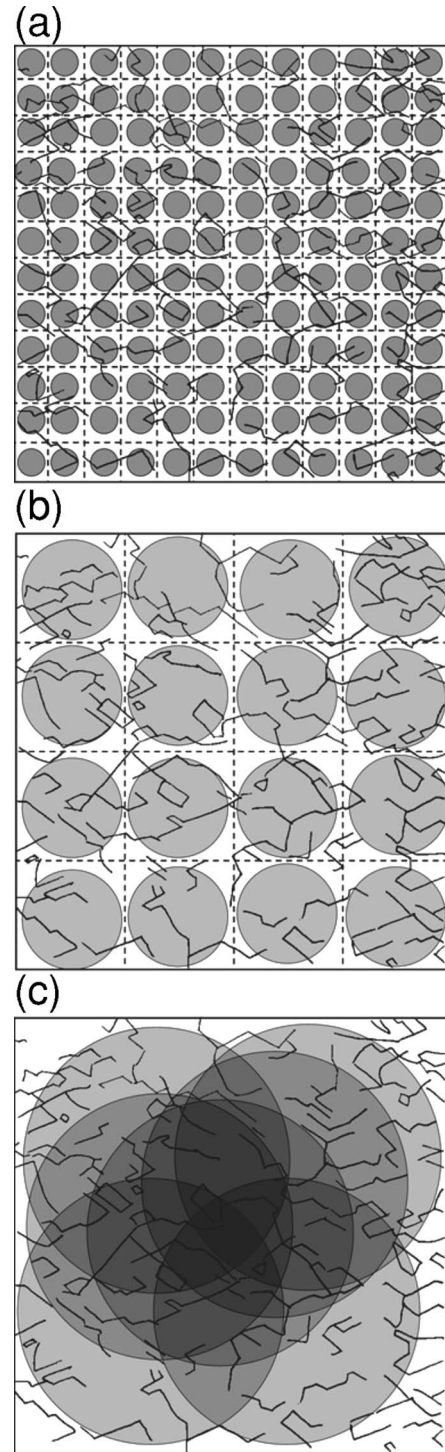

FIG. 7. Principle of fractal dimension measurement using gyration radius. For small enough radius R_D, the initial image is divided in subimages of size R_D. One single disk is set within each subimage [(a) and (b)]. For the larger disks, overlapping is allowed to achieve better statistics (c).

length scale of the APB network as the gyration radius l_0 at the crossover between the two regimes (see Fig. 8). The evolution of l_0 as a function of the film thickness is reproduced in Fig. 9. l_0 is found to increase roughly as the square root of
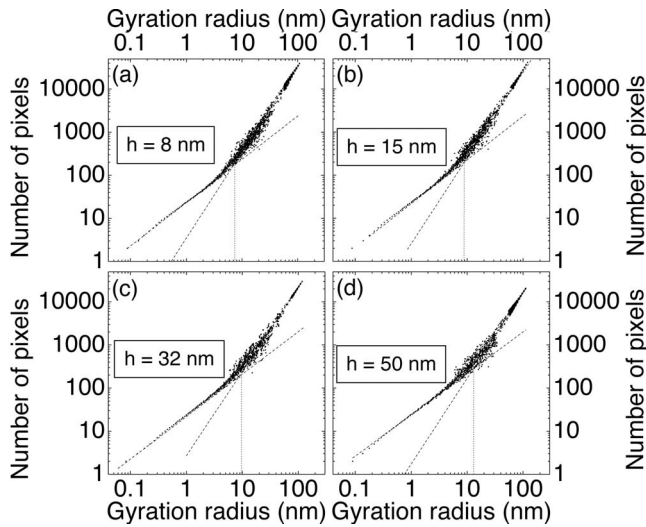
FIG. 8. Examples of fractal analysis for four different films thicknesses: number of pixels N as a function of the radius of gyration R_g plotted in a log-log scale. Dashed lines correspond to power law fits, the exponent being close to 1 before the crossover and to 2 after it (see Table I). Dotted lines indicate the characteristic length of the APB network, defined as the gyration radius at the crossover.

the film thickness and to be about 2.75 times smaller than the mean APD size $\bar{D}$.

E. APB density

The simplest measurement of the APB density from a TEM micrograph consists in summing the pixel values (the value of the pixels corresponding to APBs is 1 while the others correspond to 0) and normalizing the sum by the image area. However, this procedure may not be statistically significant given the limited scope of a given TEM image. The relevance of this measurement relies on the observation of two dimensions for the APB network and on dimension $d_{f,2}$ after the crossover. Indeed, if $\rho(R)$ stands for the density calculated from a circle of radius R and $N(R)$ the number of pixel corresponding to APBs, one gets (see the Appendix for detailed calculation):

$$\rho(R) = \frac{N(R)}{\pi R^2} \sim R^{d_{f,2}-2}. \tag{7}$$

TABLE I. Fractal dimensions before ($d_{f,1}$) and after ($d_{f,2}$) the crossover. Statistical uncertainty is the standard deviation of the measured dimension for a given film.

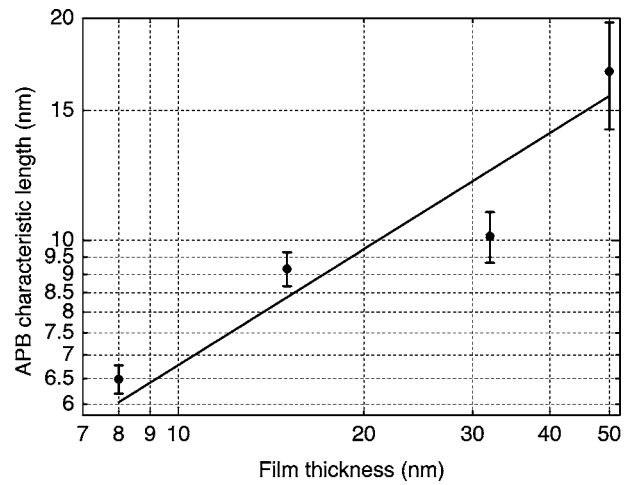| Film thickness (nm)	$d_{f,1}$	$d_{f,2}$
8	1.03±0.02	2.00±0.01
15	1.07±0.02	2.06±0.04
32	1.00±0.02	1.96±0.01
50	0.97±0.02	1.98±0.02
mean value	1.02±0.04	2.00±0.04

FIG. 9. APB characteristic length scale l_0 as a function of the film thickness (axes are logarithmic). Error bars correspond to the standard deviation calculated from the analysis of various images of the same sample. The straight line represents the best power law fit, characterized by an exponent of 0.5±0.15.

The method is thus accurate in our case, but it is worth noting that physical systems exhibiting $d_{f,2} \neq 2$ (e.g., magnetic domain walls in disordered thin films[55] or crystals exhibiting dendritic growth[56]) do exist. In such cases, the density can not be properly defined, since it depends on the image size.

In order to achieve better statistics, ρ was evaluated using a large number of circles of radius $R > l_0$ and defined as the mean value. Figure 10 represents APB density as a function of film thickness for the four films studied here. This APB density decreases roughly as one over the square root of the film thickness. The statistical variations are not due to uncertainty on ρ for a given image (the procedure used on each image leads to a statistical error below 1%), but are probably

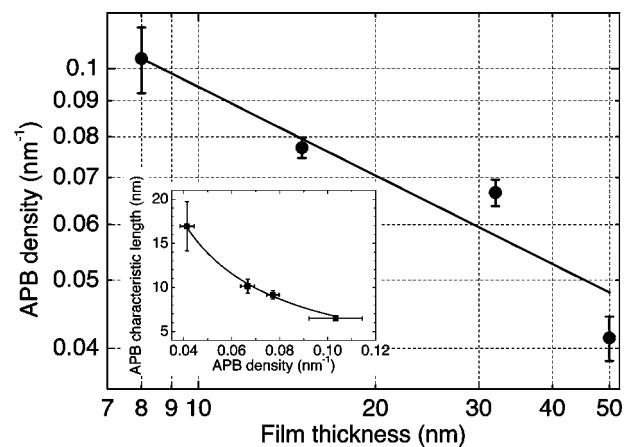FIG. 10. APB density as a function of film thickness, represented using a log-log scale. Error bars correspond to the standard deviation calculated from the density measured on several images of the same sample. The straight line represents the best power law fit, with a −0.4±0.1 exponent. Inset: APB characteristic length as a function of APB density. The line correspond to a power law fit with a fixed −1 exponent.

artifacts due to image acquisition, though slight inhomogeneities within the samples originating from local variations of fluxes, temperature, and substrate preparation cannot be ruled out.

This measurement is in agreement with the variation of l_0 with respect to the film thickness: the inset of Fig. 10 shows that the APB density is indeed proportional to the inverse of APB characteristic length ($l_0 \simeq 0.7/\rho$) as expected from the topological properties of the APB network expressed by the dimensions before and after the crossover (see the Appendix).

IV. DISCUSSION

The evolution of the APB network in Fe_3O_4 thin film is a particular case of ordering process. The kinetics of domain coarsening can be described by a power law $L \sim t^z$, where L is the characteristic length of the domains, t is the time (usually counted from quenching from a high temperature disordered state) and z an exponent strongly dependent on the nature of the ordering process but independent of the dimensionality of the system or the degeneracy of the ordered state,[57,58] which for APBs is the number of variants (8 in the case of Fe_3O_4). Systems and models can be divided in two classes:[57] when the order parameter of the system is conserved during ordering (such as, for example, during homoepitaxial growth or spinodal decomposition of binary alloys), z is equal to $1/3$, while it is $1/2$ when the order parameter is not conserved (e.g., during ferromagnetic or chemical ordering).

In the present case, predicting the value of z is not straightforward since chemical ordering occurs during the Fe_3O_4 film growth. A scenario comprising possible atomic diffusion with long-range matter transportation creating the successive ordered layers of the thin film and homogenizing the concentrations in volume (conserved order parameter $L \sim t^{1/3}$) could be envisioned, but the gradient of concentrations it requires are unlikely given the homogeneity of the incoming atomic fluxes onto the sample. Chemical ordering by local exchange of two atoms resulting in a displacement of the APBs (nonconserved order parameter $L \sim t^{1/2}$) is much more likely. From a practical point of view, the kinetics is eventually limited by the process with the lowest exponent, and experimental measurement should be able to plainly discard the conserved order parameter scenario ($L \sim t^{1/3}$).

As shown in Figs. 6 and 9, both the mean APD size $\bar{D}$ and the APB characteristic length l_0 evolves roughly as the square root of the film thickness h. Since the growth rate is kept constant for all the samples, these two lengthscales are found to increase as $t^{1/2}$, t standing here for the deposition time. The same evolution of the APD size has been observed for Fe_3O_4 (100) thin films grown on MgO (100) substrates,[35] an identical behavior being obtained when considering deposition and annealing time. The very same $z=1/2$ exponent has also been found both for bulk chemically ordered bimetallic alloys[30] and in the presence of a surface.[59,60]

The limiting process of the domain coarsening is thus the chemical ordering process over the Fe sublattices ($z=1/2$). In addition, two distinct time scales ought to be considered in

our case since domain coarsening takes place during film growth. The kinetics of bulk chemical ordering depends on a prefactor related to (usually lacunar) volume diffusion while nucleation-growth ordering on the surface bring into play surface diffusion which is a much faster process (for copper alloys, the activation energy for surface diffusion is typically of a few tenth of eV, to be compared to $1-2$ eV for volume diffusion via a lacunar mechanism). During its formation, each atomic layer would adapt very quickly to the already formed film. The time scale of this adaptation would be well below the one for the completion of a monolayer (about one minute in our case). Chemical ordering begin after coalescence of the very first layers, the ultrathin Fe_3O_4 film thus formed acting as a template. The mechanisms of domain coarsening would then be the same as in bulk bimetallic alloys, where it has been shown that the driving force behind the motion of APBs is their local curvature, kinetics being independent of the energy cost of APBs.[31]

The effective large scale fractal dimension close to 2 observed during the Fe_3O_4 film thin growth is in agreement with such a scenario: this value of the fractal dimension is obtained for random spatial distributions of nucleation center of APDs as expected at the very first time of the film growth. Moreover, the fractal dimension expected in the absence of any clustering and/or self-organization within the APB network[54] is also 2. The observed $1/2$ exponent appears as an intrinsic property of APD coarsening, regardless of the substrate onto which Fe_3O_4 is grown, but the *initial* size distribution is fixed during the first steps of growth and is linked to the density of nucleation centers. Hence, both initial Markovian APDs nucleation and APDs growth processes play a role in the APDs network geometry.

Given the slow kinetics of domain coarsening (in the growth conditions used here, the mean APD size $\bar{D}$ doubles in about 2 h), only limited increase of the characteristic antiphase domain size can be gained through thermal treatment of the film using experimentally realistic amounts of time. Annealing alone shall thus not allow to obtain single-domain devices since the APD sizes reported here or in the literature are in the tens of nm range, i.e., while the devices patterned by the standard optical lithography techniques are 2 to 3 orders of magnitude larger. From a strictly structural point of view, significant gain in the APD size is to be sought in a dramatic increase of the island size (i.e., a decrease of the density of nucleation center) by changing the growth conditions (temperature, and especially ambient pressure). However, the quite narrow range of growth conditions leading to Fe_3O_4 imposes severe limitations.

We now focus on the link between the magnetic properties of the samples and the measured APB density ρ. Within the hypothesis of the magnetic model,[49] the b factor is expected to be proportional to the APB density. Indeed, if the linear chains are independent, the magnetic moment loss is supposed to be proportional to the total APB surface. Thus the magnetization loss is proportional to the APB surface divided by the sample volume, which is the APB density discussed in Sec. III E. This linear dependency is not experimentally observed: combining the power laws evidenced in Figs. 3 and 10, we find that the b parameter evolves roughly as $\rho^{1/3}$.
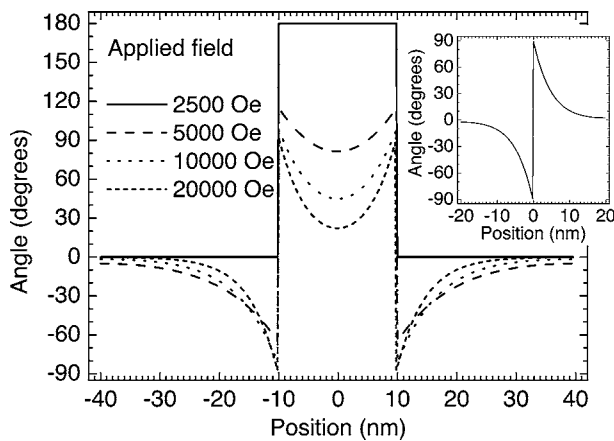
FIG. 11. Micromagnetic simulation of the magnetization profile (the origin of angles refers to the field direction) of a linear chain containing two APBs separated by $d=20$ nm. The inset shows the result of the micromagnetic simulation for a single APB under a 20 kOe applied field.

The origin of this discrepancy is to be found in the rather short APB characteristic length (see Fig. 9) and the large proportion of small APD cuts (see Fig. 5): the validity of the hypothesis of independent one-dimensional chains has to be evaluated. This has been done by considering one-dimensional chains containing two APBs. Since no simple analytical solutions exist for such systems, we solved the problem numerically with a program originally developed to simulate through energy minimization the magnetization profiles of thin films considered as one-dimensional systems.[61] The bulk values were used for Fe_3O_4 saturation magnetization $(M_0=480$ kA m$^{-1})$ and effective exchange stiffness $(A_F=10^{-6}$ erg cm$^{-1}=10^{11}$ J m$^{-1})$.[51] The simulations does not consider the field direction with respect to the crystallographic axes of Fe_3O_4 since the magnetic anisotropy is neglected as in the analytical model.

An important difference between the analytical model used in Sec. III A and the micromagnetic simulations has to be pointed out: whereas the magnetization profile given by the analytical model (which considers *infinite* chains) does not depend on the antiferromagnetic coupling A_{AF} at the APB, this is no longer true when the energy minimization is performed on *finite* chains. We have tested several values of A_{AF} with chains containing one single APB. The b parameter depends strongly on A_{AF} but not much on the chain length provided it exceeds 20 nm.

A_{AF} was finally set to -3×10^{-6} erg cm$^{-2}=-3\times10^{-9}$ J m^{-2} which leads to a b parameter in the same range as the values obtained on experimental curves reported in Fig. 3. Given the strong dependency of b on A_{AF}, this value can be considered as a reliable order of magnitude, which is comparable to the one obtained by Kalev and Nielsen.[48] As can be seen in the inset of Fig. 11, spins far from the APB are aligned with the applied field, and the typical width of the domain wall created by the APB is a few tens of nanometers. The shape of the magnetization profile is very similar to the one obtained from the analytical model which uses infinite chains.

We then used this set of parameters to simulate the magnetic behavior of chains containing two APBs. The length of
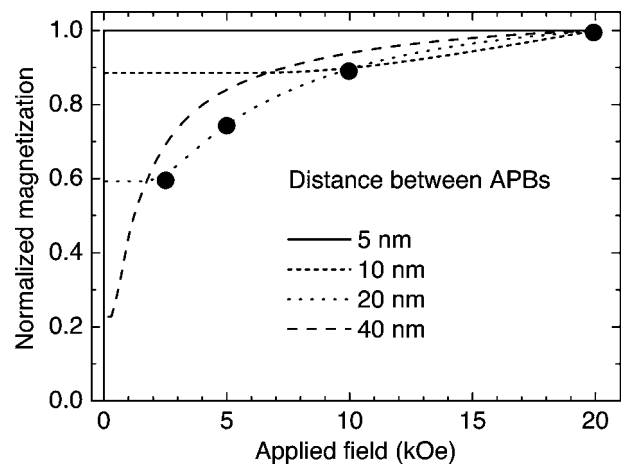

FIG. 12. Micromagnetic simulation of magnetization curves of linear chains containing two APBs separated by $d=5$, 10, 20, or 40 nm [magnetization is normalized by $M(20$ kOe) in each case]. The four black disks correspond to the configurations displayed in Fig. 11.

the "external" chains was set to 30 nm and the length of the "middle" chain, noted d was varied between 5 and 40 nm. Figure 11 shows some magnetization profiles obtained for $d=20$ nm. For sufficiently large fields, the shape of the curve away from the APB is similar to the one obtain for one single APB, but the angle between the field and the spins at the APBs is no longer 90°. Simulation for larger d (not shown here) do not show this latter trend, and APBs can be considered as independent when they are more than 40 nm apart.

To sum up, the effect of adding a second APB in the chain figures presented in Figs. 11 and 12, is twofold.

(i) For H smaller than a blocking field H_B, it stabilizes magnetic configurations consisting of homogeneous domains separated by sharp domain walls (solid line of Fig. 11). In this regime, the system exhibits a constant magnetization. It is worth noting that the blocking field is very large for the smallest value of d (it exceeds 20 kOe for $d=5$ nm).

(ii) For H larger than H_B, the magnetization can be fitted using Eq. (2). The parameter b is then found to decrease when d is increased.

Point (i) invites us to consider an effective APB density, not counting those which are too close to eachother. The fraction of "inactive" APBs is given by statistical distribution of APB cut such as the one reproduced in Fig. 5 and is thus thickness dependent. However, we believe that the influence of this effect on the b parameter is not direct, for the fraction of inactive APB is small for all the films studied in this paper. For example, even considering that all APBs exhibit antiferromagnetic coupling (which is not a valid hypothesis[47]), only about 10% of the APBs of 8-nm-thick films are less than 5 nm apart from another, and this proportion further decreases for thicker films. This variation of the *effective* APB density cannot account for the dampening of the ρ dependence of the b parameter. The existence of homogeneous, antialigned domains even at high fields may nonetheless partly explain the magnetization loss observed in all the films.[38]

Point (ii) suggests an enhanced dependency of b on ρ. Yet the b enhancement is only observed for $H>H_B$, and such

curves exhibit reduced b when fitted within the same range as the experimental data displayed in Fig. 2. Indeed, linear combinations of such curves can be very satisfactorily fitted using Eq. (2) with a b parameter lower than b's (defined in each case for $H > H_B$) of all individual curves. We believe that this indirect influence of point (i) is the main driving force of the dampening of the $b(\rho)$ curve.

V. CONCLUSION

In this paper, we have studied the properties of the antiphase boundary (APB) network of Fe_3O_4 thin films epitaxially grown onto $\alpha-Al_2O_3$ (0001) substrates, and its influence on the magnetic properties of the samples. The approach to saturation of the films has been analyzed within the framework of a one-dimensional model.[38,49] The virgin magnetization curves are satisfactorily reproduced by the model, following $M = M_0(1 - b/\sqrt{H})$. The b parameter varies as $h^{-0.15}$ where h is the film thickness. The statistical properties of the APB network were then thoroughly studied from TEM micrographs. A correlation between shift vector and boundary plane was evidenced. This anisotropy of the network, together with the extremely broad distribution of antiphase domain size make the method of domain cut at first questionable, and a fractal analysis has been further used to extract the APB characteristic length l_0, which was found to vary as $h^{1/2} \propto t^{1/2}$, that is the universal exponent for a nonconserved order parameter ordering process. The fractal dimensions observed on all the films ensure that the APB density is properly defined and varies as l_0^{-1}. This analysis also demonstrates that the coarsening of antiphase domains is a purely random phenomenon. We have finally interpreted the magnetic results, and especially the weak dependance of b in the APB density ρ with the help of micromagnetic simulations which give the order of magnitude of the magnetic coupling at the boundary ($A_{AF} = -3 \times 10^{-6}$ erg cm^{-2} = -3×10^{-9} J m^{-2}) and shows that the rather small characteristic length of the APB network (in the 10 nm range) dampens the ρ dependence of b.

ACKNOWLEDGMENTS

APPENDIX: BOUNDARY DENSITY, CHARACTERISTIC LENGTH, AND FRACTAL DIMENSIONS

Let us consider a set of domains, the boundaries exhibiting two fractal dimensions $d_{f,1}$ and $d_{f,2}$ as in Fig. 8. We choose a set of N_d disks of radius R and center O_j (R is large enough so that it corresponds to the second regime) in which we will calculate both boundary density and gyration radius. We define $\langle \cdots \rangle_j$ as the mean value taken on all the disks of radius R. For a given disk labeled j, the gyration radius is defined as $\langle G_j M_i \rangle_i$, where the M_i are the N_j points included in the disk and G_j their center of mass. Provided we have

enough disks, and since the centers of the disks are randomly chosen, we have

$$\langle R_g \rangle_j = \langle \langle G_j M_i \rangle_i \rangle_j \simeq \langle \langle O_j M_i \rangle_i \rangle_j. \tag{A1}$$

Equation (A1) can be rewritten explicitly:

$$\langle \langle O_j M_i \rangle_i \rangle_j = \frac{1}{N_d} \sum_{j=1}^{N_d} \frac{1}{N_j} \sum_{i=1}^{N_j} O_j M_i. \tag{A2}$$

Since R is large, we can rewrite Eq. (A2) using integrals

$$\langle \langle O_j M_i \rangle_i \rangle_j = \frac{1}{N_d} \sum_{j=1}^{N_d} \frac{1}{N_j} \int_0^R \int_0^{2\pi} r n_j(r,\theta) r\, dr\, d\theta, \tag{A3}$$

where $n_j(r,\theta)$ is the local APB density. We can replace the n_j's by a mean function $\bar{n}$, which is constant since N is large and the center of the disks are randomly chosen:

$$\bar{n} = \frac{\langle N_j \rangle_j}{\pi R^2}. \tag{A4}$$

We thus have

$$\langle \langle O_j M_i \rangle_i \rangle_j = \frac{1}{N_d} \sum_{j=1}^{N_d} \frac{1}{N_j} \int_0^R r \bar{n} 2\pi r\, dr = \frac{1}{N_d} \sum_{j=1}^{N_d} \frac{1}{N_j} \frac{2\pi \bar{n} R^3}{3}. \tag{A5}$$

We finally have

$$\langle \langle O_j M_i \rangle_i \rangle_j = \left\langle \frac{1}{N_j} \right\rangle_j \times \frac{2R}{3} \times \langle N_j \rangle_j \simeq \frac{2R}{3}. \tag{A6}$$

Thus R_g and R are proportional provided the disks used to calculate R_g be large enough. The boundary density is then defined as $\rho(R) = N(R)/\pi R^2$ where $N(R)$ is the average number of points in disks or radius R. Provided R is larger than l_0, $\rho(R)$ can be written as [we write $N(R) = A R_g^{d_{f,2}}$, see Eq. (6)]:

$$\rho(R) = \frac{N(R)}{\pi R^2} = \frac{N(R)}{\pi \left(\frac{3}{2} R_g\right)^2} \simeq \frac{4 A R_g^{d_{f,2}}}{9\pi R_g^2} \simeq \frac{4A}{9\pi} R_g^{d_{f,2}-2} \sim R^{d_{f,2}-2}. \tag{A7}$$

Hence, the boundary density generally depends on R, and is defined solely when $d_{f,2} = 2$. Let us now compare ρ with the characteristic length of the boundary network, defined by the crossover between $d_{f,1}$ and $d_{f,2}$ regimes in $N(R_g)$ curves

$$A l_0^{d_{f,2}} = B l_0^{d_{f,1}}. \tag{A8}$$

While A may vary with the thickness of the film under scrutiny, B is a constant once the image resolution has been taken into account. If $d_{f,2} = 2$, we can rewrite the APB density as

$$\rho = \frac{4A}{9\pi} = \frac{4B l_0^{d_{f,1}-2}}{9\pi}. \tag{A9}$$

The boundary density thus varies as l_0^{-1} only if the dimension of the network before the crossover is 1.

*Present address: Laboratoire de Physique des Matériaux, Université Henri Poincaré, 54500 Vandœuvre-les-Nancy, France. Electronic address: alexandre.bataille@lpm.u-nancy.fr

†Present address: Laboratoire Léon Brillouin, UMR 012 CEA-CNRS, CEA Saclay, F-91191 Gif-sur-Yvette, France.

[1] B. Dieny, V. S. Speriosu, S. S. P. Parkin, B. A. Gurney, D. R. Wilhoit, and D. Mauri, Phys. Rev. B **43**, 1297 (1991).

[2] J. S. Moodera, L. R. Kinder, T. M. Wong, and R. Meservey, Phys. Rev. Lett. **74**, 3273 (1995).

[3] A. Gupta and J. Z. Sun, J. Magn. Magn. Mater. **200**, 24 (1999).

[4] S. A. Wolf, D. D. Aschwalom, R. A. Buhrman, J. M. Daughton, S. von Molnar, M. L. Roukes, A. Y. Chtchelkanova, and D. M. Treger, Science **294**, 1488 (2001).

[5] M. Bowen, A. Barthelemy, M. Bibes, E. Jacquet, J.-P. Contour, A. Fert, F. Ciccacci, L. Duo, and R. Bertacco, Phys. Rev. Lett. **95**, 137203 (2005).

[6] J. S. Parker, S. M. Watts, P. G. Ivanov, and P. Xiong, Phys. Rev. Lett. **88**, 196601 (2002).

[7] J.-H. Park, E. Vescovo, H. J. Kim, C. Kwon, R. Ramesh, and T. Venkatesan, Phys. Rev. Lett. **81**, 1953 (1998).

[8] M. Bowen, M. Bibes, A. Barthélémy, J.-P. Contour, A. Anane, Y. Lemaître, and A. Fert, Appl. Phys. Lett. **82**, 233 (2003).

[9] M. Bibes, K. Bouzehouane, A. Barthélémy, M. Besse, S. Fusil, M. Bowen, P. Seneor, J. Carrey, V. Cros, A. Vaurés, J.-P. Contour, and A. Fert, Appl. Phys. Lett. **83**, 2629 (2003).

[10] A. M. Bataille, J.-B. Moussy, F. Paumier, S. Gota, M.-J. Guittet, M. Gautier-Soyer, P. Warin, P. Bayle-Guillemaud, P. Seneor, K. Bouzehouane, and F. Petroff, Appl. Phys. Lett. **86**, 012509 (2005).

[11] A. M. Bataille, A. Tagliaferri, S. Gota, C. de Nadaï, J.-B. Moussy, M.-J. Guittet, K. Bouzehouane, F. Petroff, M. Gautier-Soyer, and N. B. Brookes, Phys. Rev. B **73**, 172201 (2006).

[12] R. A. de Groot and K. H. J. Buschow, J. Magn. Magn. Mater. **54-57**, 1377 (1986).

[13] A. Yanase and K. Siratori, J. Phys. Soc. Jpn. **52**, 312 (1984).

[14] A. Cheng, M. L. Klein, and L. J. Lewis, Phys. Rev. B **44**, 13 319 (1991).

[15] H. Takahashi, S. Soyea, J. Hayakawa, K. Ito, A. Kida, C. Yamamoto, H. Asano, and M. Matsui, J. Appl. Phys. **93**, 8029 (2003).

[16] E. Snoeck, Ch. Gatel, R. Serra, G. BenAssayag, J.-B. Moussy, A. M. Bataille, M. Pannetier, and M. Gautier-Soyer, Phys. Rev. B **73**, 104434 (2006).

[17] X. W. Li, A. Gupta, G. Xiao, W. Qian, and V. P. Dravid, Appl. Phys. Lett. **73**, 3282 (1998).

[18] H. Matsuda, M. Takeuchi, H. Adachi, M. Hiramoto, N. Matsukawa, A. Odagawa, K. Setsune, and H. Sakakima, Jpn. J. Appl. Phys., Part 1 **41**, 387 (2002).

[19] G. Hu, R. Chopdekar, and Y. Suzuki, J. Appl. Phys. **93**, 7516 (2003).

[20] G. Hu and Y. Suzuki, Phys. Rev. Lett. **89**, 276601 (2002).

[21] K.-I. Aoshima and S. X. Wang, J. Appl. Phys. **93**, 7954 (2003).

[22] P. J. van der Zaag, P. J. H. Bloemen, J. M. Gaines, R. M. Wolf, P. A. A. van der Heijden, R. J. M. van de Veerdonk, and W. J. M. de Jonge, J. Magn. Magn. Mater. **211**, 301 (2000).

[23] P. Seneor, A. Fert, J.-L Maurice, F. Montaigne, F. Petroff, and A. Vaurès, Appl. Phys. Lett. **74**, 4017 (1999).

[24] K. Ghosh, S. B. Ogale, S. P. Pai, M. Robson, E. Li, I. Jin, Z.-W. Dong, R. L. Greene, R. Ramesh, T. Venkatesan, and M. Johnson, Appl. Phys. Lett. **73**, 689 (1998).

[25] A. M. Bataille, R. Mattana, P. Seneor, A. Tagliaferri, S. Gota, K. Bouzehouane, C. Deranlot, M.-J. Guittet, J.-B. Moussy, C. de Nadaï, N. B. Brookes, F. Petroff, and M. Gautier-Soyer, J. Magn. Magn. Mater. (to be published).

[26] A. Bataille, Ph.D. thesis, Université Paris XI, 2005 (in French).

[27] D. T. Margulies, F. T. Parker, F. E. Spada, R. S. Goldman, J. Li, R. Sinclair, and A. E. Berkowitz, Phys. Rev. B **53**, 9175 (1996).

[28] D. T. Margulies, F. T. Parker, M. L. Rudee, F. E. Spada, J. N. Chapman, P. R. Aitchison, and A. E. Berkowitz, Phys. Rev. Lett. **79**, 5162 (1997).

[29] A. J. Ardell, N. Mardesich, and C. N. J. Wagner, Acta Metall. **27**, 1261 (1979).

[30] J. W. Cahn, Scr. Metall. **14**, 93 (1980).

[31] S. M. Allen and J. W. Cahn, Acta Metall. **27**, 1085 (1979).

[32] O. van der Biest and G. Thomas, Phys. Status Solidi A **24**, 65 (1974).

[33] A. G. Fitzgerald and T. G. May, Thin Solid Films **35**, 201 (1976).

[34] F. C. Voogt, T. Fujii, P. J. M. Smulders, L. Niesen, M. A. James, and T. Hibma, Phys. Rev. B **60**, 11193 (1999).

[35] W. Eerenstein, T. T. M. Palstra, T. Hibma, and S. Celotto, Phys. Rev. B **68**, 014428 (2003).

[36] J.-F. Bobo, D. Basso, E. Snoeck, C. Gatel, D. Hrabovsky, J. L. Gauffier, L. Ressier, R. Many, S. Visnovsky, J. Hamrle, J. Teilet, and A. R. Fert, Eur. Phys. J. B **24**, 43 (2001).

[37] M. Ziese and H. J. Blythe, J. Phys.: Condens. Matter **12**, 13 (2000).

[38] J.-B. Moussy, S. Gota, A. Bataille, M.-J. Guittet, M. Gautier-Soyer, F. Delille, B. Dieny, F. Ott, T. D. Doan, P. Warin, P. Bayle-Guillemaud, C. Gatel, and E. Snoeck, Phys. Rev. B **70**, 174448 (2004).

[39] C. Gatel, Ph.D. thesis, INSA Toulouse, France, 2004 (in French).

[40] C. Gatel and E. Snoeck (in preparation).

[41] V. V. Rodatis, D. S. Su, C. Kuhrs, W. Ranke, and R. Schögl, Thin Solid Films **396**, 78 (2001).

[42] W. Eerenstein, Ph.D. thesis, University of Gröningen, 2003.

[43] S. Celotto, W. Eerenstein, and T. Hibma, Eur. Phys. J. B **3**, 6 271 (2003).

[44] J. B. Goodenough, *Magnetism and the Chemical Bond* (Wiley and Sons, New York, 1963), Vol. 1.

[45] J. Kanamori, J. Phys. Chem. Solids **10**, 87 (1959).

[46] P. W. Anderson, *Magnetism* (Academic Press, New York, 1963), Vol. 1.

[47] T. Kasama, R. E. Dunin-Borkowski, and W. Eerenstein, Phys. Rev. B **73**, 104432 (2006).

[48] L. A. Kalev and L. Niesen, Phys. Rev. B **67**, 224403 (2003).

[49] B. Dieny, D. Givord, and J. M. B. Ndjaka, J. Magn. Magn. Mater. **93**, 503 (1991).

[50] S. Gota, J.-B. Moussy, M. Henriot, M.-J. Guittet, and M. Gautier-Soyer, Surf. Sci. **482-485**, 809 (2001).

[51] Q. Pan, T. G. Pokhil, and B. M. Moskowitz, J. Appl. Phys. **9**, 1 5945 (2002).

[52] T. Hibma, F. C. Voogt, L. Nielsen, P. A. A. van der Heijden, W. J. M. de Jonge, J. J. T. M. Donkers, and P. J. van der Zaag, J. Appl. Phys. **85**, 5291 (1999).

[53] L. Potez and A. Loiseau, Interface Sci. **2**, 91 (1994).

[54] J. Feder, *Fractals* (Plenum, New York, 1988).

[55] J.-P. Attané, Y. Samson, A. Marty, J. C. Toussaint, G. Dubois, A. Mougin, and J.-P. Jamet, Phys. Rev. Lett. **93**, 257203 (2004).

[56] A. L. Barabasi and H. E. Stanley, *Fractal Concepts in Surface Growth* (Cambridge University Press, Cambridge, 1995).

[57] A. J. Bray, Adv. Phys. **43**, 357 (1994).

[58] Y. Enomoto and R. Kato, J. Phys.: Condens. Matter **2**, 9215 (1990).

[59] S. Goapper, L. Barbier, B. Salanon, A. Loiseau, and X. Tolleres, Phys. Rev. B **57**, 12497 (1998).

[60] E. Le Goff, D. Le Floc'h, L. Barbier, S. Goapper, B. Salanon, and A. Loiseau, Phys. Rev. B **63**, 125418 (2001).

[61] F. Montaigne, S. Mangin, and Y. Henry, Phys. Rev. B **67**, 144412 (2003).